Effects of CVD direct growth of carbon nanotubes and nanofibers on microstructure and electrochemical corrosion behavior of 316 stainless steel

Mazdak Hashempour[*], *Antonello Vicenzo*[1], *Fu Zhao*[2], *Massimiliano Bestetti*[3]

Dipartimento di Chimica, Materiali e Ingegneria Chimica "Giulio Natta", Politecnico di Milano, Via L. Mancinelli 7, 20131 Milan, Italy

Received 17 September 2013
Received in revised form
13 February 2014
Accepted 1 March 2014

1. Introduction

Chemical vapor deposition (CVD) has been recognized as a versatile and robust method to synthesize carbon nanotubes (CNTs) and carbon nanofibers (CNFs) on different substrates [1]. Considering the variety of applications in which CNTs can be exploited due to their outstanding mechanical, optical, electrical and electrochemical properties [2], remarkable attention has been paid to CVD as a facile and reliable synthesis method of this material [3]. Basically, CVD uses a controlled atmosphere containing a carbonaceous species at a suitable temperature to decompose the carbon precursor on a catalytic surface and subsequently, by supersaturating the catalyst particle, makes the extra carbon to precipitate in a certain crystalline form, namely,

[*] *Corresponding author*. Tel.: +39 334 728 4631; fax: +39 02 23993180.
E-mail addresses: mazdak.hashempour@gmail.com, mazdak.hashempour@mail.polimi.it (M. Hashempour), antonello.vicenzo@polimi.it (A. Vicenzo), fu.zhao@mail.polimi.it (F. Zhao), massimiliano.bestetti@polimi.it (M. Bestetti).

graphite [4]. In this regard, proper preparation of the catalyst layer on the surface of the substrate to be covered by CNTs is a vital step. Accordingly, the availability of substrate materials showing catalytic activity for CNT synthesis translates into an effective facilitation of the synthesis by elimination of a crucial step, namely, catalyst preparation, and therefore, to economic justification as well [5]. From this standpoint, stainless steel, as an economic material with a high content of iron as the catalyst for CNT synthesis, is an interesting candidate. In fact, several groups have conducted research on direct growth of CNT on stainless steel [6–23]. Generally, the interest behind this area of research is multiple, including electrodes for supercapacitors [24–26], sensor technology [27–30], fuel cells [31,32], batteries [33], catalyst support for wastewater treatment [10], field emission probes [34–38] and low friction applications [39–41]. Obviously, many of these applications are related to electrochemical performance of a stainless steel/CNT electrode or, in any instance, may imply exposure to aggressive environments. Accordingly, the investigation on the corrosion behavior of such materials is a necessary step to confirm their viability for those applications. However, to the best of the authors' knowledge, an in-depth study on the corrosion response of stainless steel/CVD grown CNT has not been performed yet.

This work thus aims to explore the changes in the substrate caused by the CNT growth which then may affect its corrosion behavior, as expected in view of the well-established vulnerability of stainless steel to corrosion upon high temperature exposure to carbon rich environments [42–45]. More precisely, this work is intended to investigate the corrosion behavior of 316 stainless steel coated with different types of filamentous carbon materials, namely, CNT and CNF, directly grown on the substrate by CVD method. Since these types of conductive carbon do not form a dense and compact layer, the occasion is offered for studying the effects of CNT/CNF growth conditions on the corrosion behavior of stainless steel. Electrochemical testing for corrosion assessment was conducted under conditions simulating the working environment of bipolar plates (BPs) in polymer electrolyte membrane fuel cells (PEMFCs) [31]. Actually, the highly corrosive environment in which BPs should work, namely high acidity and relatively high temperature, makes this instance stand out as an upper limit in terms of the severity of the corrosion conditions within the aforementioned applications. Hence, any possible weakness of the system which could not possibly appear in milder corrosion conditions was more likely to be revealed herein.

2. Experimental

2.1. Growth of CNT and CNF on Stainless Steel

Stainless steel (type 316) plates of the size 15 × 15 × 1 mm were used as the substrate. Careful cleaning, including 10 min sonication in acetone and 10 min sonication in distilled water followed by nitrogen drying, was applied to all samples to remove organic and inorganic contaminants. Then, samples were transferred to the CVD reactor.

The synthesis procedure of CNT/CNFs on 316 SS was described in detail in earlier works [6]. Briefly, filamentous carbon was directly grown on the surface of 316 SS in a CVD reactor by catalytic decomposition of ethylene (C_2H_4). The 316 SS substrate catalyzes ethylene decomposition at the process temperature of 760 °C, so that it was used without the deposition of any additional catalyst. A quartz tube (diameter = 20 mm) heated in a horizontal tubular furnace was used as the CVD reactor. Reactive and carrier gases were delivered to the reactor through mass flow controllers. For CNT growth, the tube was primarily purged with a mixed flow of nitrogen and hydrogen to reduce the surface oxide during the temperature ramp-up to 760 °C. After stabilization of the temperature, ethylene was introduced to the reactor. Flow rates of N_2, H_2 and C_2H_4 during the growth step were 100, 6, and 20 sccm, respectively. The detailed process cycle for the growth of CNT is described in Table 1. In the case of CNF growth, the first step was the oxidation of the steel substrate in air, without any control by shielding or reducing gases. The furnace temperature was ramped up to 800 °C for oxidation and then reduced to 760 °C. After purging the reactor with nitrogen to remove air, a reduction step followed under mixed flow of hydrogen and nitrogen for 30 min. The CNF growth step was finally performed under the same flow rate conditions as for CNT. The detailed process cycle for the growth of CNF is described in Table 2. The mass gain of the samples (hereafter referred to as deposited carbon) was calculated from the mass difference before and after the CVD treatment by using a Sartorius M2P electronic microbalance with an accuracy of 0.001 mg.

Finally, to study the effect of the CVD process temperature on the electrochemical behavior of the sample in the absence of any carbonaceous gas, a series of 316 SS samples were treated in the tubular furnace under the same thermal and atmospheric conditions mentioned in Table 1 for CNT growth, but without ethylene admission.

2.2. Electrochemical Characterization and Corrosion Tests

The corrosion behavior of coated and uncoated samples was studied by performing potentiodynamic and potentiostatic tests, using a standard three-electrode cell set-up, in 1 M H_2SO_4 + 2 ppm HF solution, at 80 °C. As the working electrode, different samples were used, namely, the bare as-received 316 SS, nitrogen heat treated 316 SS (SS-NH) and CNT or CNF coated 316 SS. A platinum coated titanium sheet was used as the counter electrode and a saturated calomel electrode (SCE) as the reference electrode. Electrochemical tests were conducted using a ModuLab system (Solartron Analytical).

Table 1 – CNT growth process cycle in the CVD reactor.

Steps	Temp (°C)	Duration (min)	Atmosphere
1. Heat-up	25 to 760	49	N_2 (100 sccm) H_2 (6 sccm)
2. Stabilization	760	10	N_2 (100 sccm) H_2 (6 sccm)
3. Growth	760	20	N_2 (100 sccm) H_2 (6 sccm) C_2H_4 (20 sccm)
4. Cool-down	760 to 25	140 (approximately)	N_2 (100 sccm) H_2 (6 sccm)

Table 2 – CNF growth process cycle in the CVD reactor.

Steps	Temp (°C)	Duration (min)	Atmosphere
1. Heat-up	25 to 800	52	Air (atm. pressure)
2. High temp. oxidation	800	10	Air (atm. pressure)
3. Nitrogen purging & stabilization	760	15	N_2 (200 sccm)
4. Reduction	760	30	N_2 (100 sccm) H_2 (50 sccm)
5. Growth	760	20	N_2 (100 sccm) H_2 (6 sccm) C_2H_4 (20 sccm)
6. Cool-down	760 to 25	140 (approximately)	N_2 (100 sccm) H_2 (6 sccm)

Potentiodynamic experiments were performed in the potential range from −0.5 to 1 V vs. SCE at a scan rate of 1 mV s^{-1} in deaerated electrolyte saturated with nitrogen. Potentiostatic tests were carried out at potentials of −0.1 V and 0.6 V vs. SCE in an H_2 or O_2 saturated electrolytes, respectively, in the attempt to simulate the polarization conditions of the cathode and anode in a real fuel cell system [46–48]. Before each experiment, samples were left immersed in the electrolyte for 60 min to allow equilibration with the corrosive environment. Open circuit potential (OCP) measurements in all cases showed a steady trend.

2.3. *Microstructural Characterization*

In order to identify the compounds present or formed at the surface or near surface region at different processing steps, the crystal structure of as-grown and corroded samples was studied by grazing incidence X-ray diffraction (XRD) technique with a 1830 PW Philips X-ray generator, equipped with a PW 3020 Philips goniometer and a PW 3710 Philips control unit. The radiation used was Cu Kα, with a scan step time of 0.50 s and a step size (2θ) of 0.02° with the sample in the thin film geometry arrangement at 0.5° glancing angle and rotating detector. The same instrument was used to study the as-received samples in Bragg–Brentano geometry.

Microstructural characterizations of as-received, as-grown and corroded samples were carried out by scanning electron microscope, SEM, using either a Zeiss EVO 50 EP equipped with energy dispersive X-ray, EDX, or a Stereoscan 360 Cambridge SEM instrument.

3. Results and Discussion

3.1. *Microstructural Characterization*

Fig. 1a and b presents SEM micrographs of CNT and CNF samples directly grown on the stainless steel substrate, respectively. It is seen that CNTs are thin and their diameter size does not vary in a wide range. However, the presence of a small fraction of CNFs can be seen as individual filaments of larger diameter. Small catalyst particles can also be observed on the tips of CNTs as tiny bright spots. The morphology of these nanoparticles as well as the multiwalled carbon nanotubes (MWCNTs) grown on 316 SS was investigated by transmission electron microscopy, as reported elsewhere [6]. From the observation of a population of CNTs, it is confirmed that the number of walls is about 25 to 30, with an inner diameter of 10 ± 2 nm and an outer diameter of 40 ± 10 nm. CNFs, in contrast, show a range of diameter size, from 60 to hundreds of nanometers, and are characterized by the presence of a large number of catalyst particles at the tip of the filaments. The deposited carbon mass was measured to be 0.5 mg cm^{-2} for CNTs and 2–4 mg cm^{-2} for CNFs. The CNF carpet was quite thick (10–30 μm) while the CNT one was much thinner (1–3 μm). Although individual CNTs were as long as several micrometers, their entangled arrangement did not result in the formation of a thick layer.

Fig. 2 shows the XRD patterns of different samples. XRD pattern of pristine 316 SS reveals the peaks of austenite, as expected. Moreover, weak reflections of a thin surface oxide

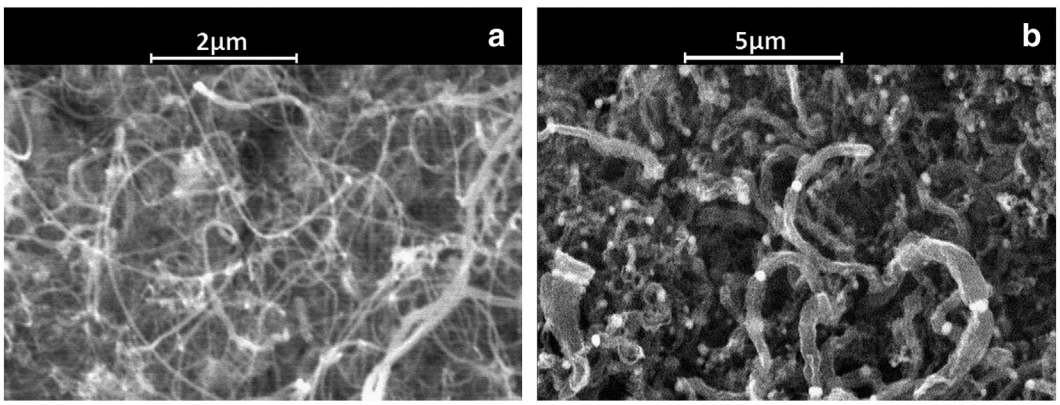

Fig. 1 – SEM micrographs of as-grown samples showing (a) CNTs and (b) CNFs.

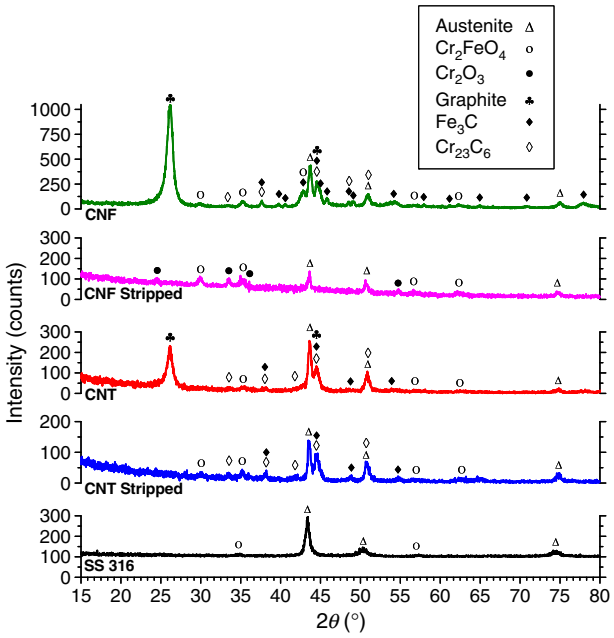

Fig. 2 – XRD patterns of as-received and as-grown samples.

film are recognized. The pattern marked as "CNT" refers to a CNT coated 316 SS sample and in fact shows the characteristic peaks of the austenite phase and the peaks of hexagonal graphite at 2θ values of 26.09° and 44.57°, corresponding to the (002) and (101) reflections. The pattern labeled "CNF" in Fig. 2 refers to a CNF coated 316 SS sample. More intense graphite peaks in CNF sample can be related to both the much higher mass of deposited material and the structure of CNF, with graphene platelets perpendicular to or inclined at a small angle to the fiber axis, forming "stacked" or "herring-bone" structures, respectively [49]. In addition to filamentous carbon, it can be inferred from the XRD patterns that the high temperature synthesis in the presence of ethylene resulted also in the formation of chromium and iron carbides — the latter more obvious for the case of CNF growth. In this respect, it may be inferred that the surface modifications caused by the oxidation–reduction pretreatment used for CNF synthesis resulted in an enhanced formation of iron carbide. Actually, at variance with CNT samples, XRD pattern of CNF samples showed relatively strong reflections of chromium and iron oxides.

In the event that Fe_3C and possibly other carbide particles were trapped in the CNT/CNF layers, as it may be in view of their potential involvement in the mechanism of carbon nanotube and fiber growth [50–57], an attempt was made to separate the possible contribution of carbide particles within the layer, e.g. at the tip of carbon filaments, from those due to substrate carburization. For this purpose, the carbon layer was removed by gently shaving the surface with a plastic blade, followed by mild cleaning of the stainless steel surface with a tissue. This procedure was used for both CNT and CNF samples in order to perform the XRD analysis on the stripped substrate after exposure to the CVD processing environment. The absence of graphite peaks in the patterns labeled "Stripped" in Fig. 2 confirms that the carbon layer was effectively removed from the substrate, though, as revealed by SEM surface micrographs of the samples in Fig. 3, a small amount of filaments remained in the grooves, but apparently could not be detected by XRD. A further remark is that while chromium carbide was still detected after stripping of the CNT layer (see pattern "CNT Stripped" in Fig. 2), iron and chromium carbide reflections disappeared from the XRD pattern of the CNF sample. Hence, notwithstanding the possibility of the presence of traces of carbide in the CNT Stripped sample – undetectable by XRD due to the low amount or the masking effect of a surface oxide – it can be safely concluded that the Fe_3C formed during the synthesis of CNF was to a large extent incorporated within the carbon layer in the form of particles on the tip of filaments, which is in good agreement with the SEM observations (Fig. 1b).

3.2. *Electrochemical Behavior*

3.2.1. *Potentiodynamic Tests*

Fig. 4 shows potentiodynamic curves for the different samples in deaerated 1 M H_2SO_4 + 2 ppm HF electrolyte at 80 °C. The potentiodynamic curves show obvious and marked differences. As a preliminary remark, it can be noticed that there were only relatively small changes in the free corrosion potential for coated samples, compared to the bare substrate (E = −0.328 V vs. SCE for bare 316 SS, E = −0.325 V vs. SCE for SS-NH, E = −0.314 V vs. SCE for CNT on 316 SS sample and E = −0.280 V vs. SCE for CNF on 316 SS sample). The observed corrosion potential is apparently the potential resulting from the coupling of the hydrogen reduction and iron oxidation reactions, irrespective of the presence of the filamentous carbon coatings and the surface modifications of the substrate during the growth process. This observation can be understood in the light of the porous nature of the layers. The slight higher value measured for the CNF sample is probably related to the oxidation of the surface, as revealed by XRD.

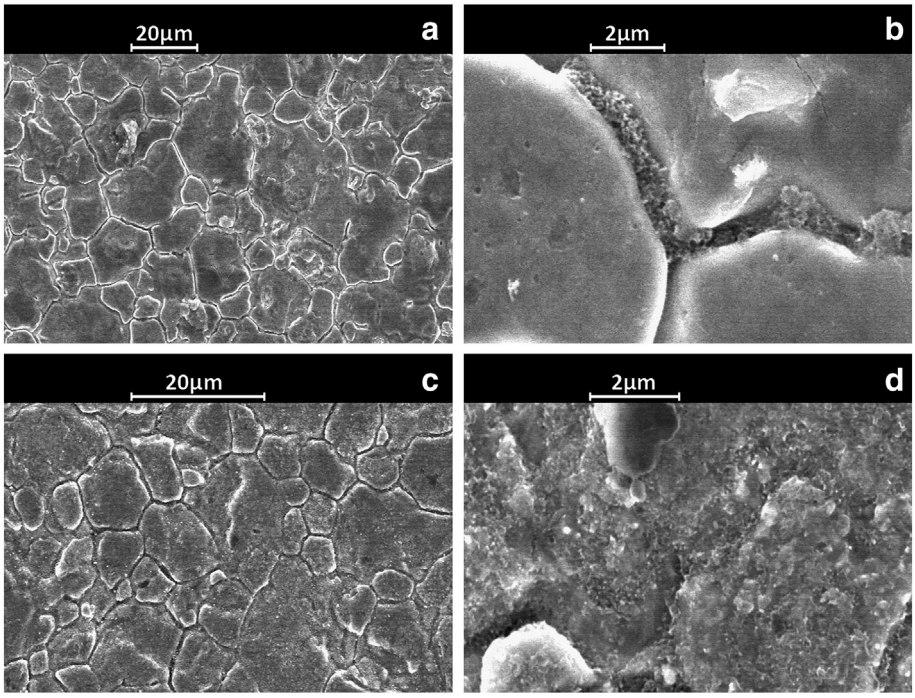

Fig. 3 – SEM micrographs of 316 SS substrates stripped from (a, b) CNT and (c, d) CNF.

The Tafel extrapolation method [58] was used to calculate the corrosion current density (c.d.). The c.d. derived from this method is higher for both the CNT and CNF coated samples compared to that of the bare steel, namely: about 15×10^{-4}, and 20×10^{-4} A cm^{-2}, compared to 5×10^{-4} A cm^{-2}, respectively. Moreover, over almost all the anodic region above the free corrosion potential, coated samples show a much higher anodic c.d. which is indicative of high susceptibility to corrosion. In this regard, at both potentials of −0.1 V and 0.6 V vs. SCE, corresponding to the anodic and cathodic polarizations of BPs, respectively, these materials will be liable to rapid attack.

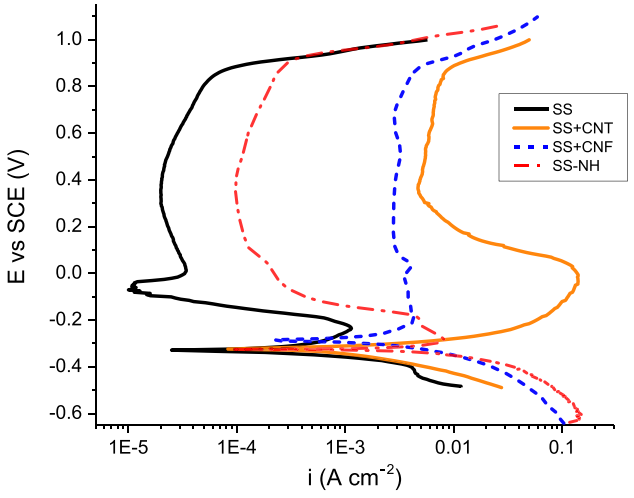

Fig. 4 – Potentiodynamic curves of 316 SS, 316 SS + CNT, 316 SS + CNF and SS-NH samples in 1 M H_2SO_4 + 2 ppm HF solution at 80 °C. (For interpretation of the references to color in this figure, and other color containg figures, the reader is referred to the web version of this article.)

Interestingly, the anodic c.d. of SS-NH in the passive region lies between that of the pristine 316 SS and those of CNT/CNF coated samples. This increase of the dissolution rate in the passive potential region obviously points to the susceptibility of SS to sensitization [59] upon exposure to the high temperature of CNT growth, independently of the presence of a carburizing environment. However, the increase of the c.d., though remarkable compared to bare 316 SS, is still far below the high anodic c.d. of CNT/CNF coated samples, suggesting that the carburizing atmosphere strongly aggravates the effects of heat treatment in CNT/CNF coated samples.

3.2.2. *Potentiostatic Tests*

The electrochemical behavior was further characterized by performing potentiostatic experiments, see Fig. 5, under conditions similar to those used to simulate anodic and cathodic environments in polymer electrolyte fuel cells, i.e., in 1 M H_2SO_4 + 2 ppm HF electrolyte, saturated with H_2 or O_2 and at −0.1 V or 0.6 V vs. SCE, respectively, at 80 °C. For the sake of brevity, these will be referred to in the following as anodic and cathodic conditions or environments.

The results of the potentiostatic test under anodic conditions are presented in Fig. 5a, also for a stripped sample along with bare stainless steel, and CNT or CNF coated 316 SS samples. The anodic c.d. of the bare 316 SS decays rapidly at the beginning reaching a value in the range of 10^{-5} A cm^{-2} after 1000 s. A steady state is then established, followed by a slow gradual decrease of the c.d. through an oscillating behavior and a faster reduction after about 10 000 s, when the c.d. decreases down to about 10^{-6} A cm^{-2} (level 1 in Fig. 5). CNT or CNF coated samples, as well as the corresponding so-called

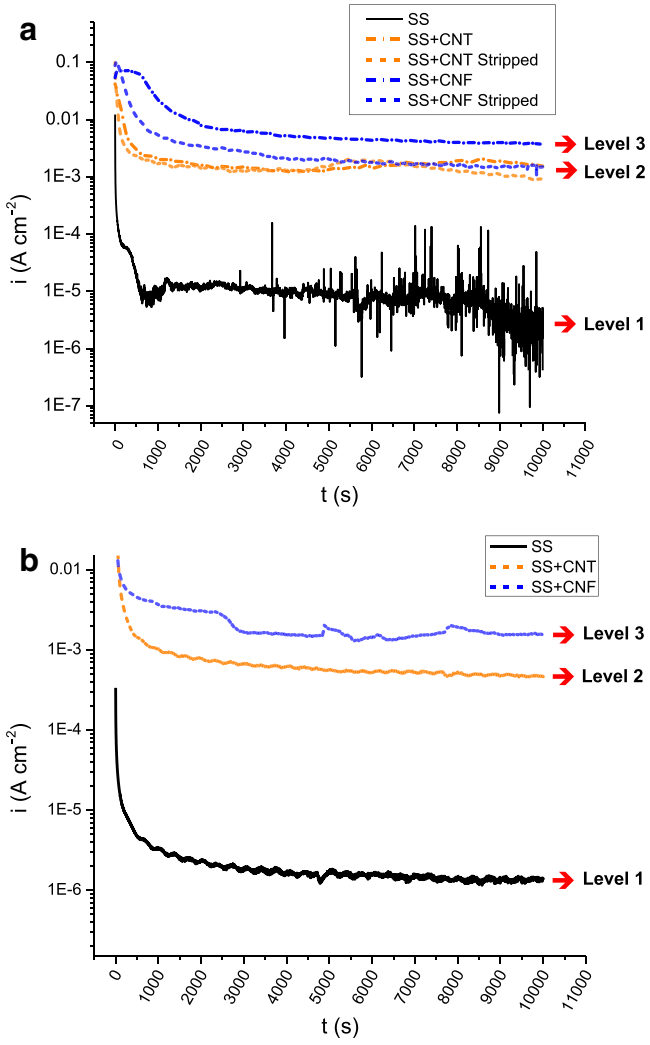

Fig. 5 – Potentiostatic curves of 316 SS, 316 SS + CNT and 316 SS + CNF samples in 1 M H_2SO_4 + 2 ppm HF solution at 80 °C, (a) saturated with H_2, at −0.1 V vs. SCE, and (b) saturated with O_2, at 0.6 V vs. SCE.

stripped samples, show c.d. almost three orders of magnitude higher, in the range of 10^{-3} A cm^{-2}, with minor but significant differences. Namely, two different levels of dissolution c.d. can be observed: for the CNT coated and stripped samples (level 2 in Fig. 5); and for the CNF coated sample (level 3 in Fig. 5).

Fig. 5b shows the results of potentiostatic tests for the cathodic environment. The general behavior of the samples is similar to that observed in the anodic environment, meaning that there are three different levels of c.d., the lowest referring to pristine 316 SS (in the range of 10^{-6} A cm^{-2}), and orders of magnitude higher values for both coated samples. The highest c.d., about 2×10^{-3} A cm^{-2}, is found for the CNF on 316 SS sample (level 3), while the CNT on 316 SS sample stands somewhat lower at about 5×10^{-4} A cm^{-2} (level 2). SS-NH samples subjected to potentiostatic tests (not shown here) confirmed the behavior revealed by the potentiodynamic polarization; namely, a steady dissolution c.d. of about 1.5×10^{-5} A cm^{-2} and 8.0×10^{-5} A cm^{-2}, respectively under the conditions simulating the cathodic and anodic environments, was observed for the SS-NH sample.

3.3. Microstructural Characterization After Potentiostatic Tests

The effects of potentiostatic polarization tests were looked into by performing XRD and SEM characterizations of the samples. XRD patterns of as-prepared and stripped CNT and CNF samples on 316 SS after testing under anodic conditions are collected in the graph of Fig. 6.

CNF sample which had the maximum amount of filamentous carbon shows depressed peaks of graphite even after corrosion, which means that in some areas the CNF carpet still remains on the surface. The CNT sample, however, seems to have lost almost the entire CNT layer. Furthermore, XRD results indicate that oxides (typically Cr_2O_3 and Fe_3O_4) formed at the surface of all these samples. Apparently, the oxidation was stronger on the unstripped CNF corroded sample, particularly due to the formation of Fe_3O_4. Significantly, the Fe_3C phase disappeared after anodic testing, suggesting the formation of iron oxide by dissociation of the carbide under the aggressive corrosion conditions [60]. In support of the latter view is the observation that only CNF samples showed clear evidence of

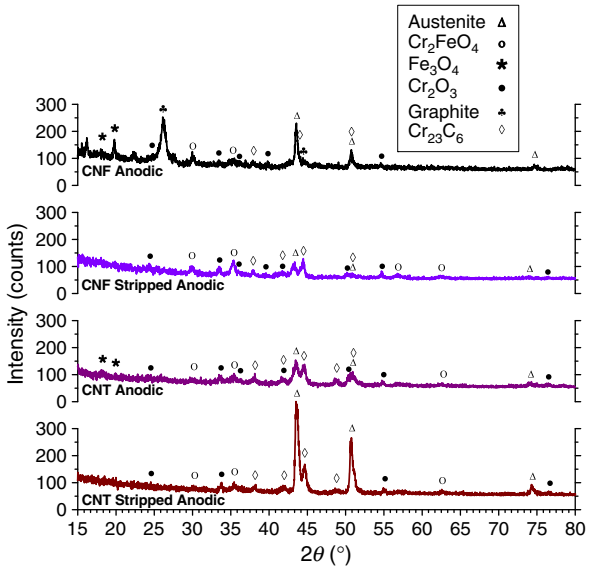

Fig. 6 – XRD patterns of corroded samples.

the presence of Fe_3C. Besides, since the Fe_3O_4 was found only on the surface of unstripped samples, the Fe_3C source responsible for its formation had to be already present in the CNF layer.

In the light of the XRD results of corroded samples, the behavior observed under potentiostatic polarization can be explained in more detail. The about three orders of magnitude increase of the c.d. (so called level 2) compared to pristine 316 SS (level 1) is mostly related to the effect of the carburization of the steel substrate on its corrosion resistance. Further evidence in this respect is given in the following section. A further increase in the dissolution c.d. (level 3) is mainly caused by the oxidation of the Fe_3C incorporated in the CNF layer over the 316 SS substrate. Though the presence of oxidizable particles in the CNT layer cannot be ruled out, it is reasonably assumed, according to SEM results (Fig. 1a), that their overall mass, and consequently their contribution to the c.d. during potentiostatic tests, was negligible. Accordingly, the c.d. for CNT sample corrosion remains at level 2 and only CNF sample with a significant amount of iron carbide and possibly metal particles trapped in the layer (Fig. 1b) will show higher c.d. (level 3).

SEM micrographs of 316 SS after potentiostatic test in simulated anodic environment are shown in Fig. 7. Although strong, the electrochemical attack was homogeneous and uniform all over the surface and local deep attacks could not be observed.

Fig. 8 shows the SEM micrographs of CNT on 316 SS after 10000 s potentiostatic corrosion test under the anodic environment conditions. Fig. 8a shows a general view of the surface of the sample with three different areas highlighted: in area 1, the boundary between corroded and uncorroded regions; in area 2, the surface of the substrate beneath the CNT layer; and in area 3, a severely damaged region with evidence of penetrating intergranular attack and grain removal from the substrate. From the magnified view of area 1 in Fig. 8b, the accumulation of corrosion products within the CNT layer is apparent. The substrate beneath the CNT layer (area 2, shown in Fig. 8c) exhibits obvious features due to preferential attack at grain boundary and in fact, locally, grain removal. A magnified view of area 3 is shown in Fig. 8d, with highlighted regions "e" and "f" presented in Fig. 8e and f, respectively. The presence of a layer of corrosion products can be noticed on the surface of the grains, within the area where grain removal has not occurred yet (like the one marked as "f" in Fig. 8d). This is a porous and relatively thick layer apparently enveloping the grains, thus allowing for a comparatively faster intergranular attack and the ensuing grain removal. Besides, this film, which forms below the CNT layer, is likely responsible for the loss of adhesion of the CNT layer and its progressive detachment from the surface. The appearance of the grains in the damaged area (like the one marked as "e" in Fig. 8d) can be understood as a result of the relatively slow formation of the surface layer following the detachment of grains.

Fig. 9 shows the SEM micrographs of a CNF sample after 10000 s potentiostatic corrosion test under the anodic environment conditions. As can be seen in Fig. 9a, the three regions characterizing the effects of corrosion on the CNT sample are present also in this sample. However, an extra layer marked as "0" is noticed here which did not form in the case of CNT coated sample. This layer, which appears rather thick and exhibits a kind of spongy morphology, is therefore a type of corrosion product only found over the CNF layer. Magnified view of this region (Fig. 9b) shows individual grains obviously removed from the stainless steel substrate and trapped within the layer. Referring to the large number and size of the nanoparticles present in CNF and absent in CNT samples, it is quite likely that layer 0 is formed by oxidation of those particles. Fig. 9c shows the CNF layer (layer 1) below the

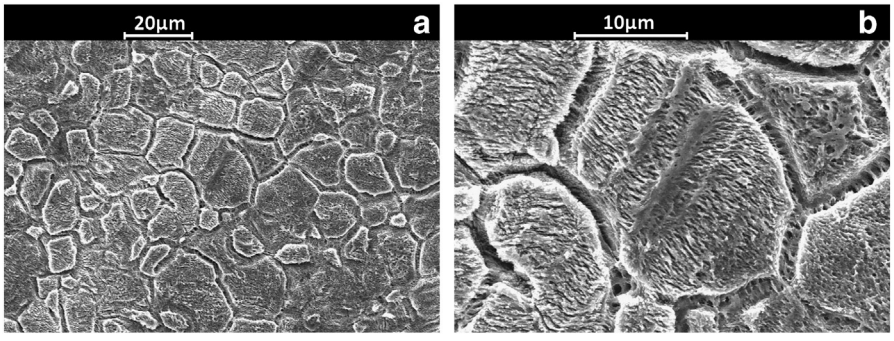

Fig. 7 – (a) SEM micrograph of 316 SS after 10000 s potentiostatic test under anodic environment conditions, (b) higher magnification of (a).

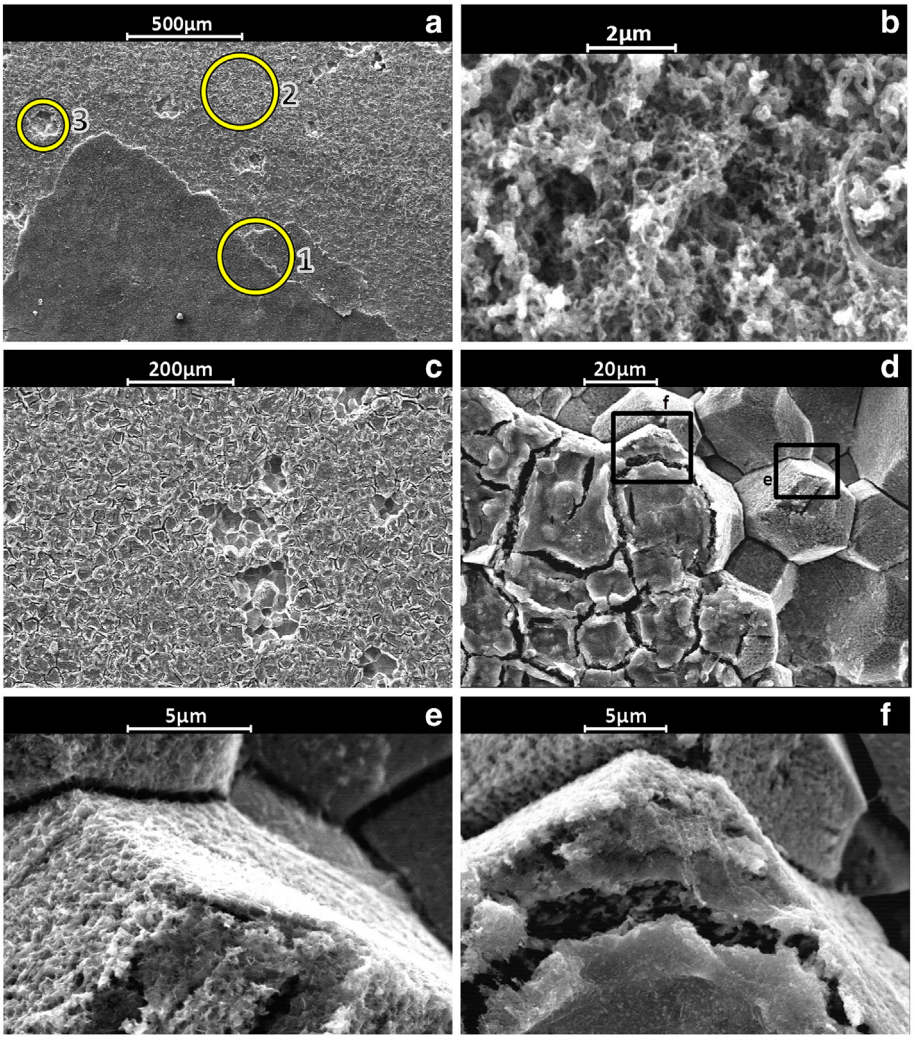

Fig. 8 – SEM micrographs of "CNT on 316 SS" sample after 10000 s potentiostatic corrosion test under the anodic environment conditions showing three different zones and different magnifications of each zone.

topmost corrosion products (layer 0). The substrate beneath the CNF carpet is seen in Fig. 9d in which grain removal and surface oxidation can be recognized. The area marked as "e" in this image shows an already detached group of grains which are magnified in Fig. 9e. The region marked as "f" in Fig. 9d concentrates on a sub-layer beneath the removed grains (area 3) and, as can be seen in the magnified view (Fig. 9f), it possesses a cleaner surface compared to the primary layer right below the CNF carpet. However, surface oxidation and formation of feather like oxides on this sub-layer is obvious. Finally, the corrosion products formed on the primary surface beneath the CNF carpet (Fig. 9g) shows similar characteristics to the same area (i.e., area 2) of CNT sample.

In order to confirm the hypothesis pointed out above, a detailed microstructural analysis was also conducted on one of the stripped samples after potentiostatic test. Fig. 10 shows the SEM micrographs of a CNT sample, stripped and subjected to potentiostatic corrosion test during a duration of 10000 s, under the anodic environment conditions. Both images of secondary and back-scattered electrons (Fig. 10a and b, respectively) reveal the same features as observed in Figs. 8 and 9 for regular samples. Darker areas in Fig. 10b suggest the formation of oxides. For a more precise evaluation of element distribution, EDS analyses were conducted in three zones as indicated in Fig. 10c. Zone 1 is the top layer of corrosion products formed on the surface that was marked as area 2 in Figs. 8 and 9. Zone 2 indicates a region where the corrosion film of zone 1 was removed but not the grains. Zone 3 represents a region where the topmost layer of grains was removed and grains from the sub-surface layers are appearing (area 3 in Figs. 8 and 9). Fig. 10d shows the EDS analysis results for elemental distribution of these three regions. As expected, region 1 shows the highest contents of chromium, carbon and oxygen and the lowest iron content. These results, accompanied by the information provided from XRD patterns, suggest that this layer is mainly composed of iron and chromium oxides. Moreover, the relatively high carbon content detected by EDS in combination with the identification of $Cr_{23}C_6$ peaks in XRD patterns, demonstrates the presence of chromium carbide in this region.

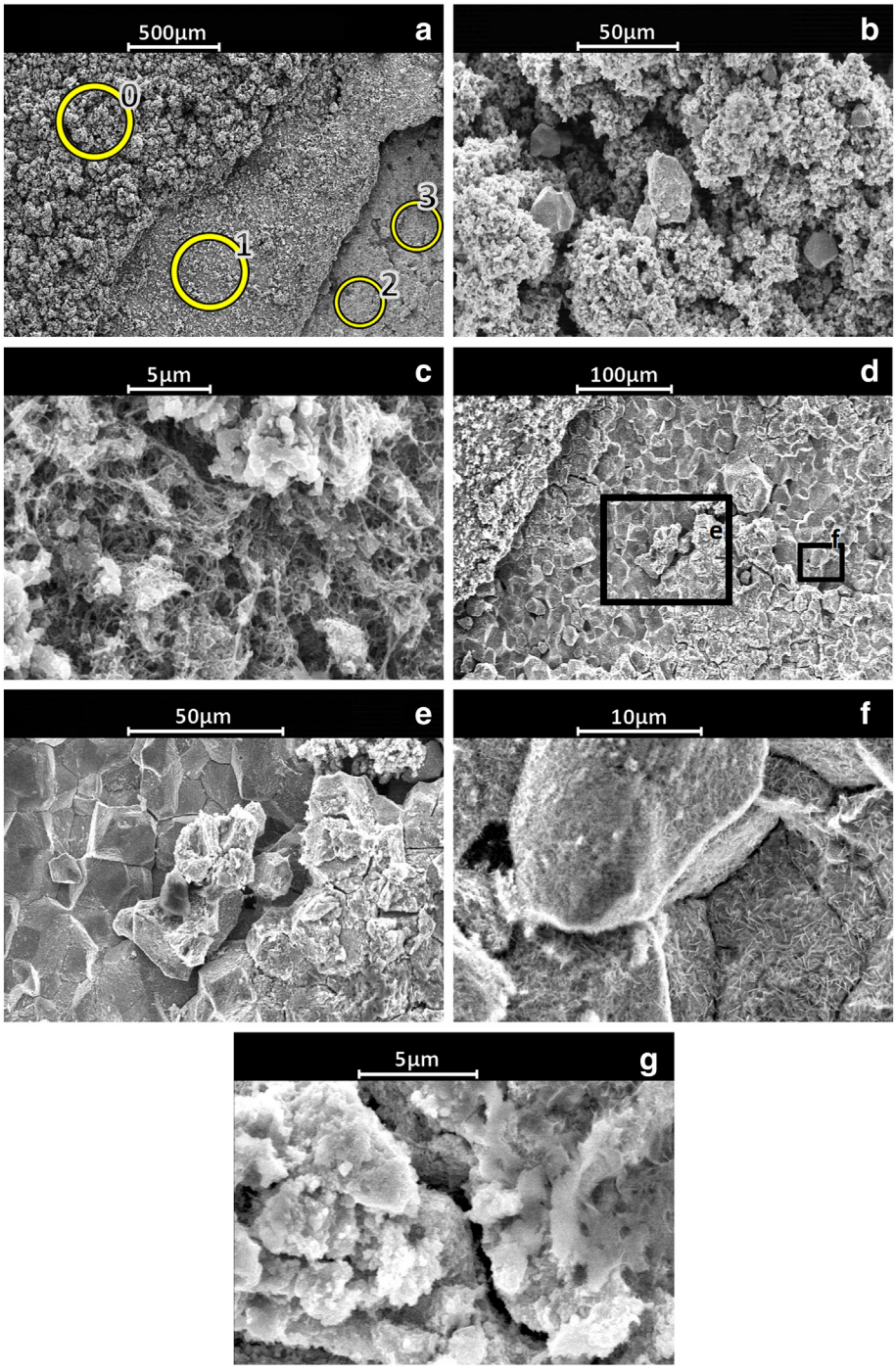

Fig. 9 – SEM micrographs of "CNF on 316 SS" sample after 10 000 s potentiostatic corrosion test under the anodic environment conditions showing four different zones and different magnifications of each zone.

Region 2 shows a much lower carbon content while the oxygen is still high, suggesting that oxidation is still considerable in this region. Region 3, which stands for the sub-layer beneath the removed grains, shows the lowest oxygen and highest iron content demonstrating the gradual decrease in oxidation intensity toward the depth of the sample. As a further remark, it is noted that the carbon content is not much decreased compared to region 2 as an indication of its penetration into the steel.

To further assess the type and intensity of the corrosion attack, the stripped CNT sample was sectioned before and after anodic potentiostatic test, mounted and etched with Nital 2% and subjected to SEM and EDS analyses. Since 316 SS cannot be etched with Nital 2% in normal condition, any probable etching would be a sign of carbide compounds formation. Fig. 11a shows the cross section SEM micrograph of the uncorroded, Nital etched sample which reveals a grain boundary etching down to the depth of about 50 µm. Fig. 11b shows the sample after potentiostatic test

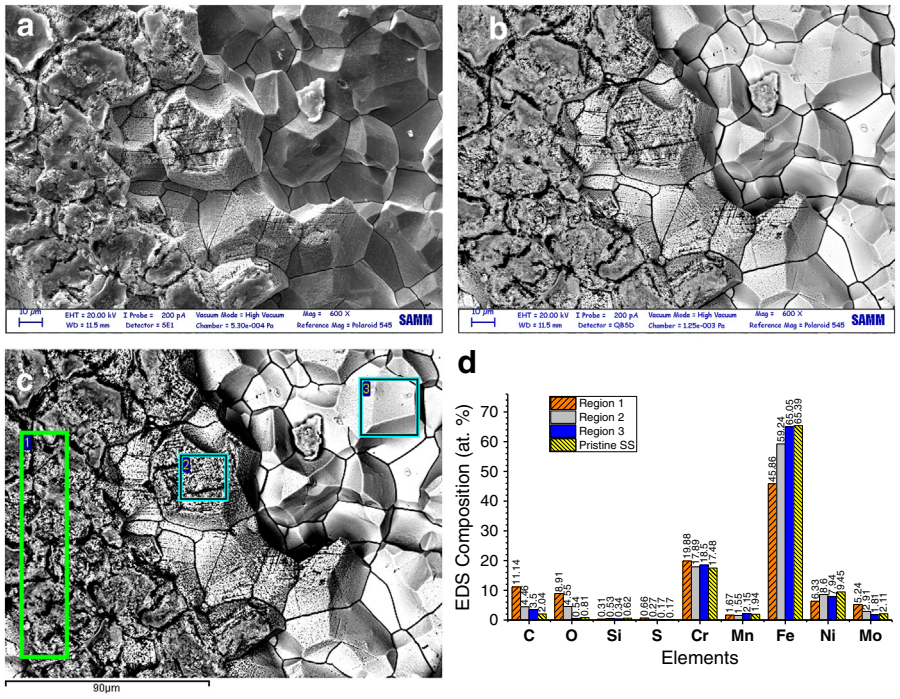

Fig. 10 – SEM micrographs of 316 SS + CNT stripped sample after 10 000 s of potentiostatic corrosion test under the anodic environment conditions. (a) Secondary electron mode, (b) back-scattered mode, (c) point analysis locations and (d) EDS results at three different zones, compared to pristine 316 SS.

without metallographic etching. It is seen that the characteristics of intergranular corrosion including boundary dissolution and grain removal are all present.

Fig. 12 shows the etched cross section of a stripped CNT sample before corrosion test. As it can be seen in Fig. 12a, a lamellar microstructure formed in the grain boundaries near the surface. To assess the elemental characteristics of this microstructure, a line scan was performed from point A to point B intersecting the lamellar structure. The results are presented in Fig. 12b showing a local modest increase in the chromium content and a decrease in the iron content with considerable and almost constant carbon content inside and outside the grain boundary. These observations reinforce the speculation that due to a sensitization like phenomenon, chromium carbide has been formed in the grain boundaries with a lamellar structure resulting in localized and accelerated corrosion.

According to the results of the above discussed microstructural observations, it can be concluded that during the CNT/CNF synthesis process, the topmost surface layer of the stainless steel substrate undergoes carbon saturation and probably carbide formation leading to CNT/CNF growth on supersaturated sites [4,50]. However, carbon can diffuse quite deep in the bulk and, of course, this diffusion would be accelerated through shortcut paths, namely, grain boundaries. These high carbon content regions would encourage chromium carbide formation in specific areas such as grain boundaries during cooling down in a quite similar way to what happens during sensitization of austenitic stainless steels [59]. Consequently, the areas depleted from chromium due to carbide formation will lose their corrosion resistance and will undergo rapid attack. Grain boundaries as the most likely places for chromium carbide precipitation

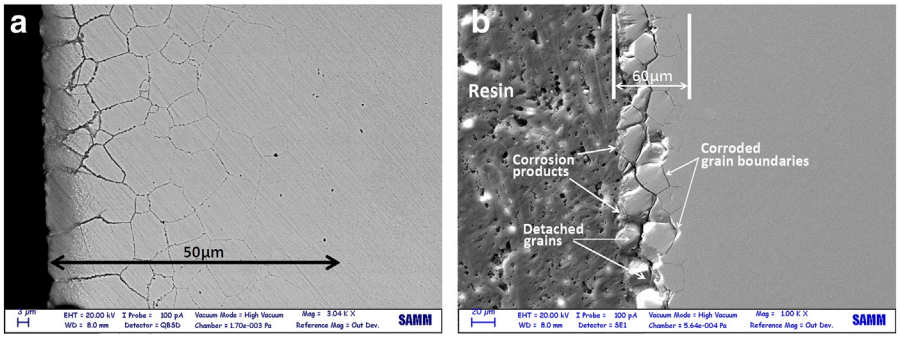

Fig. 11 – SEM micrographs of cross sectioned stripped 316 SS + CNT samples (a) etched with Nital 2% before corrosion test and (b) without etching after 10 000 s of potentiostatic corrosion test under the anodic environment conditions.

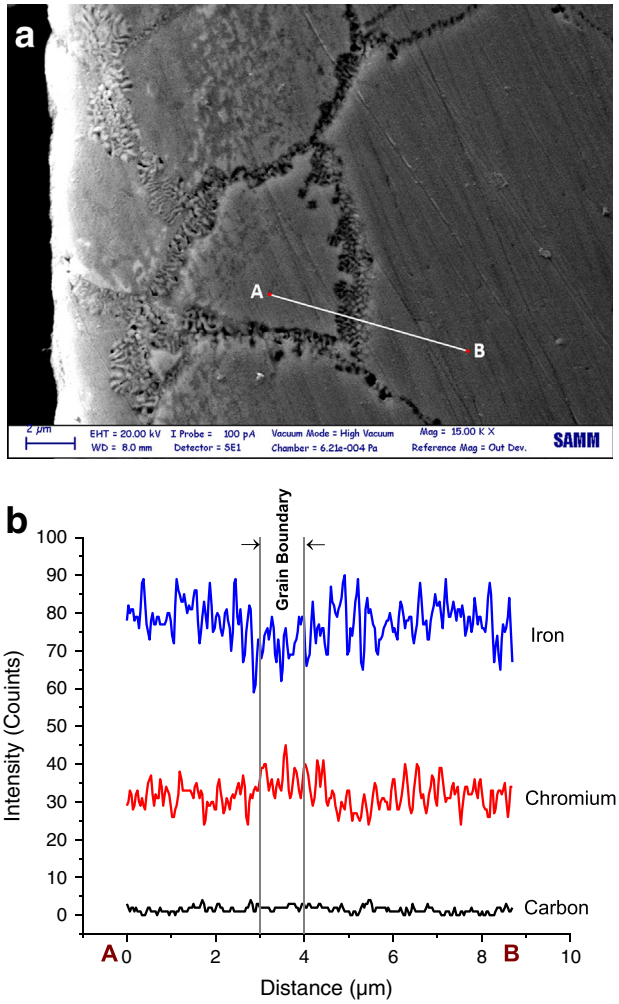

Fig. 12 – (a) SEM micrograph of an etched (Nital 2%) cross section of a stripped CNT sample before corrosion test and (b) EDS line scan results from point A to point B.

would experience the fastest corrosion rate resulting in intergranular corrosion and grain removal [61–64]. This kind of strong corrosion can be acknowledged as responsible for the large difference between dissolution c.d. of levels 1 and 2 in potentiostatic curves (Fig. 5). Since level 1 represents the corrosion rate of untreated 316 SS and level 2 represents the corrosion rate of carbon treated sample, the difference should be caused by "accelerated" intergranular corrosion. The dissolution c.d. of the sample heat treated in nitrogen, in the absence of carbonaceous gas, supposedly susceptible to normal sensitization of austenitic SS, lies well below the so-called level 2. Level 3 adds up the effects of both intergranular corrosion and oxidation of carbide and possibly metal particles trapped in the CNF layer.

4. Conclusions

CNT/CNF coatings were synthesized directly on 316 SS by CVD method without any external catalyst. The corrosion behavior of the prepared materials was investigated under simulated anodic and cathodic working conditions of BPs of PEMFCs. Based on the electrochemical and microstructural results, general corrosion behavior of such materials can be summarized as follows:

1- Potentiodynamic results show similar free corrosion potential for 316 SS, 316 SS + CNT and 316 SS + CNF samples confirming that the porous carbon layers cannot provide a barrier type protection. The three samples, 316 SS, 316 SS + CNT and 316 SS + CNF, showed corrosion current density of about 5.0×10^{-4}, 15×10^{-4} and 20×10^{-4} A cm^{-2}, respectively.
2- Potentiostatic results showed three different levels of stabilized dissolution c.d., the lowest of which (level 1) was for pristine 316 SS. The first increase in dissolution c.d. (to level 2) was related to the activation of intergranular corrosion; the final increase in the dissolution c.d. (level 3) observed only in 316 SS + CNF sample was related to the oxidation of large catalyst particles on the tips of CNFs.
3- Based on XRD, SEM and EDS results, corrosion products are mainly chromium and iron oxides. Iron carbide formed during CNF synthesis, and possibly also during CNT synthesis, though to a much minor extent, appears to undergo dissociation under strong acidic attack resulting in the oxidation of iron. On the other hand, chromium carbide formed during CNT/CNF synthesis seems to be stable, and can be observed in the XRD patterns after corrosion.

According to all above, it is concluded that the application of CNT or CNF coatings on sensitizable stainless steel by CVD direct growth method is not beneficial in terms of corrosion resistance. Since no evidence was observed suggesting the presence of a passive film, application of high temperature carbon coatings could be risky even for dense and non-porous layers especially for portable and transportation applications which are subject to mechanical shock and possible coating damage. Investigations on the growth of CNTs on heat resistant stainless steels such as high chromium content grade 310 and duplex stainless steels or stabilized grades 347 and 321 should be considered as a future research direction, to face the risk of severe damage of the base material due to carburization. Grade 310 or duplex stainless steel with high chromium content and consequently lower likelihood of grain boundary chromium depletion are supposed to provide better resistance against sensitization [65–67]. Moreover, stabilized grades 347 and 321 with strong carbide forming additives such as titanium, niobium, or tantalum, could further reduce the risk of sensitization and intergranular corrosion [68].

Acknowledgments

Authors acknowledge partial financial support from Fondazione Cariplo, through the Materiali Avanzati 2011 Program, Project 2011-0336.

The authors would also like to thank the staff of "Servizio di Analisi Microstrutturali dei Materiali" and "Laboratorio di

ingegneria delle superfici e rivestimenti avanzati" of Politecnico di Milano for their technical assistance.

REFERENCES

[1] Dupuis A-C. The catalyst in the CCVD of carbon nanotubes—a review. Prog Mater Sci 2005;50:929–61.
[2] Meyyappan M, editor. Carbon nanotubes: science and applications. Boca Raton, FL: CRC Press; 2005.
[3] Choy KL. Chemical vapour deposition of coatings. Prog Mater Sci 2003;48:57–170.
[4] Baker RTK. Catalytic growth of carbon filaments. Carbon 1989;27:315–23.
[5] Talapatra S, Kar S, Pal SK, Vajtai R, Ci L, Victor P, et al. Direct growth of aligned carbon nanotubes on bulk metals. Nat Nanotechnol 2006;1:112–6.
[6] Hashempour M, Vicenzo A, Zhao F, Bestetti M. Direct growth of MWCNTs on 316 stainless steel by chemical vapor deposition: effect of surface nano-features on CNT growth and structure. Carbon 2013;63:330–47.
[7] Hashempour M, Vicenzo A, Bestetti M. Comparative study of the growth of CNTs on stainless steel with and without the external catalyst. ECS Meet Abstr; 2013 [MA2013-02:2447–2447].
[8] Camilli L, Scarselli M, Del Gobbo S, Castrucci P, Nanni F, Gautron E, et al. The synthesis and characterization of carbon nanotubes grown by chemical vapor deposition using a stainless steel catalyst. Carbon 2011;49:3307–15.
[9] Camilli L, Castrucci P, Scarselli M, Gautron E, Lefrant S, Crescenzi MD. Probing the structure of Fe nanoparticles in multiwall carbon nanotubes grown on a stainless steel substrate. J Nanopart Res 2013;15:1–9.
[10] Sano N, Hori Y, Yamamoto S, Tamon H. A simple oxidation–reduction process for the activation of a stainless steel surface to synthesize multi-walled carbon nanotubes and its application to phenol degradation in water. Carbon 2012;50:115–22.
[11] Sano N, Kodama T, Tamon H. Direct synthesis of carbon nanotubes on stainless steel electrode for enhanced catalyst efficiency in a glucose fuel cell. Carbon 2013;55:365–8.
[12] Sano N, Yamamoto S, Tamon H. Cr as a key factor for direct synthesis of multi-walled carbon nanotubes on industrial alloys. Chem Eng J 2014;242:278–84.
[13] Baddour CE, Fadlallah F, Nasuhoglu D, Mitra R, Vandsburger L, Meunier J-L. A simple thermal CVD method for carbon nanotube synthesis on stainless steel 304 without the addition of an external catalyst. Carbon 2009;47:313–8.
[14] Baddour CE, Meunier J. Carbon nanotube synthesis on stainless steel for use in a nanotube–titanium nitride nanocomposite. 8th IEEE Conference on Nanotechnology, 2008, NANO '08; 2008. p. 752–5.
[15] Baddour CE, Upham DC, Meunier J-L. Direct and repetitive growth cycles of carbon nanotubes on stainless steel particles by chemical vapor deposition in a fluidized bed. Carbon 2010;48:2652–6.
[16] Hordy N, Mendoza-Gonzalez N-Y, Coulombe S, Meunier J-L. The effect of carbon input on the morphology and attachment of carbon nanotubes grown directly from stainless steel. Carbon 2013;63:348–57.
[17] Vander Wal RL, Hall LJ. Carbon nanotube synthesis upon stainless steel meshes. Carbon 2003;41:659–72.
[18] Sabeti Nejad N, Larijani MM, Ghoranneviss M, Balashabadi P, Shokouhy A. Direct growth of carbon nanotubes on Ar ion bombarded AISI 304 stainless steel substrates. Surf Coat Technol 2009;203:2510–3.
[19] Martínez-Hansen V, Latorre N, Royo C, Romeo E, García-Bordejé E, Monzón A. Development of aligned carbon nanotubes layers over stainless steel mesh monoliths. Catal Today 2009;147: S71–5.
[20] Ko Y-K, Lee W-B, Lee C-W, Yoo S. Nanocrystallized steel surface by micro-shot peening for catalyst-free carbon nanotube growth. Mater Res Bull 2010;45:343–7.
[21] Karwa M, Iqbal Z, Mitra S. Scaled-up self-assembly of carbon nanotubes inside long stainless steel tubing. Carbon 2006;44:1235–42.
[22] He M, Fedotov PV, Obraztsova ED, Viitanen V, Sainio J, Jiang H, et al. Chiral-selective growth of single-walled carbon nanotubes on stainless steel wires. Carbon 2012;50:4294–7.
[23] Gaikwad AV, Rout TK, Van der Plas D, Dennis RV, Banerjee S, Pacheco Benito S, et al. Carbon nanotube/carbon nanofiber growth from industrial by-product gases on low- and high-alloy steels. Carbon 2012;50:4722–31.
[24] Wang Y, Liu H, Sun X, Zhitomirsky I. Manganese dioxide–carbon nanotube nanocomposites for electrodes of electrochemical supercapacitors. Scr Mater 2009;61:1079–82.
[25] Chen YM, Cai JH, Huang YS, Lee KY, Tsai DS. Preparation and characterization of iridium dioxide–carbon nanotube nanocomposites for supercapacitors. Nanotechnology 2011;22(115706):1–7.
[26] Doerfler S, Meyer A, Althues H, Dani I, Kaskel S. Vertical aligned carbon nanotube deposition on metallic substrates by CVD. ECS Trans 2009;25:1047–51.
[27] Yun Y, Gollapudi R, Shanov V, Schulz MJ, Dong Z, Jazieh A, et al. Carbon nanotubes grown on stainless steel to form plate and probe electrodes for chemical/biological sensing. J Nanosci Nanotechnol 2007;7:891–7.
[28] Minnikanti S, Skeath P, Peixoto N. Electrochemical characterization of multi-walled carbon nanotube coated electrodes for biological applications. Carbon 2009;47:884–93.
[29] Yeow JTW, She JPM. Carbon nanotube-enhanced capillary condensation for a capacitive humidity sensor. Nanotechnology 2006;17:5441–8.
[30] Luo Y, Wal RV, Hall LJ, Scherson DA. Preparation and characterization of multiwalled carbon nanotubes grown directly onto a conducting support. Electrochem Solid-State Lett 2003;6:A56–8.
[31] Lee Y-B, Lee C-H, Lim D-S. The electrical and corrosion properties of carbon nanotube coated 304 stainless steel/ polymer composite as PEM fuel cell bipolar plates. Int J Hydrogen Energy 2009;34:9781–7.
[32] Lee Y-B, Lee C-H, Kim K-M, Lim D-S. Preparation and properties on the graphite/polypropylene composite bipolar plates with a 304 stainless steel by compression molding for PEM fuel cell. Int J Hydrogen Energy 2011;36:7621–7.
[33] Masarapu C, Subramanian V, Zhu H, Wei B. Long-cycle electrochemical behavior of multiwall carbon nanotubes synthesized on stainless steel in Li ion batteries. Adv Funct Mater 2009;19:1008–14.
[34] Lin C-L, Chen C-F, Shi S-C. Field emission properties of aligned carbon nanotubes grown on stainless steel using CH_4/ CO_2 reactant gas. Diamond Relat Mater 2004;13:1026–31.
[35] Song J, Sun M, Chen Q, Wang J, Zhang G, Xue Z. Field emission from carbon nanotube arrays fabricated by pyrolysis of iron phthalocyanine. J Phys D Appl Phys 2004;37:5–9.
[36] Wang N, Yao BD. Nucleation and growth of well-aligned, uniform-sized carbon nanotubes by microwave plasma chemical vapor deposition. Appl Phys Lett 2001;78:4028–30.
[37] Yao BD, Wang N. Carbon nanotube arrays prepared by MWCVD. J Phys Chem B 2001;105:11395–8.
[38] Sinha N, Sun Y, Yeow J. Field emission properties of carbon nanotube thin films grown on different substrate materials. 8th IEEE Conference on Nanotechnology, 2008, NANO '08; 2008. p. 270–3.

[39] Abad MD, Sánchez-López JC, Berenguer-Murcia A, Golovko VB, Cantoro M, Wheatley AEH, et al. Catalytic growth of carbon nanotubes on stainless steel: characterization and frictional properties. Diamond Relat Mater 2008;17:1853–7.
[40] Hu JJ, Jo SH, Ren ZF, Voevodin AA, Zabinski JS. Tribological behavior and graphitization of carbon nanotubes grown on 440C stainless steel. Tribol Lett 2005;19:119–25.
[41] Kaewsai D, Watcharapasorn A, Singjai P, Wirojanupatump S, Niranatlumpong P, Jiansirisomboon S. Thermal sprayed stainless steel/carbon nanotube composite coatings. Surf Coat Technol 2010;205:2104–12.
[42] Grabke HJ. Carburization: a high temperature corrosion phenomenon. St. Louis, MO: Material Technology Institute of the Chemical Process Industries; 1998.
[43] Hoyt WB, Caughey RH. High temperature metal deterioration in atmospheres containing carbon-monoxide and hydrogen. Corrosion (NACE) 1959;15:21–4 [627t–630t].
[44] Grabke HJ. Carburization, carbide formation, metal dusting, coking. Mater Tehnol 2002;36:297–305.
[45] Szakálos P. Mechanisms of metal dusting. PhD Dissertation Kungl. Tekniska Högskolan (KTH), Institutionen för Materialvetenskap; 2004.
[46] Wang H, Sweikart MA, Turner JA. Stainless steel as bipolar plate material for polymer electrolyte membrane fuel cells. J Power Sources 2003;115:243–51.
[47] Wang Y, Northwood DO. Effects of O_2 and H_2 on the corrosion of SS316L metallic bipolar plate materials in simulated anode and cathode environments of PEM fuel cells. Electrochim Acta 2007;52:6793–8.
[48] Wu J, Yuan XZ, Martin JJ, Wang H, Zhang J, Shen J, et al. A review of PEM fuel cell durability: degradation mechanisms and mitigation strategies. J Power Sources 2008;184:104–19.
[49] Teo KBK, Singh C, Chhowalla M, Milne WI. Catalytic synthesis of carbon nanotubes and nanofibers. In: Nalwa HS, editor. Encyclopedia of nanoscience and nanotechnology, vol. X. Stevenson Ranch, Calif: American Scientific Publishers; 2004. p. 1–22.
[50] Esconjauregui S, Whelan CM, Maex K. The reasons why metals catalyze the nucleation and growth of carbon nanotubes and other carbon nanomorphologies. Carbon 2009;47:659–69.
[51] Yoshida H, Takeda S, Uchiyama T, Kohno H, Homma Y. Atomic-scale in-situ observation of carbon nanotube growth from solid state iron carbide nanoparticles. Nano Lett 2008;8:2082–6.
[52] Madix RJ, Benziger J. Kinetic processes on metal single-crystal surfaces. Annu Rev Phys Chem 1978;29:285–306.
[53] Schaper AK, Hou H, Greiner A, Phillipp F. The role of iron carbide in multiwalled carbon nanotube growth. J Catal 2004;222:250–4.
[54] Yao Y, Falk LKL, Morjan RE, Nerushev OA, Campbell EEB. Synthesis of carbon nanotube films by thermal CVD in the presence of supported catalyst particles. Part II: the nanotube film. J Mater Sci Mater Electron 2004;15:583–94.
[55] Behr MJ, Mkhoyan KA, Aydil ES. Orientation and morphological evolution of catalyst nanoparticles during carbon nanotube growth. ACS Nano 2010;4:5087–94.
[56] Behr MJ, Andre Mkhoyan K, Aydil ES. Catalyst rotation, twisting, and bending during multiwall carbon nanotube growth. Carbon 2010;48:3840–5.
[57] Behr MJ, Mkhoyan KA, Aydil ES. Carbon diffusion from methane into walls of carbon nanotube through structurally and compositionally modified iron catalyst. Microsc Microanal 2011;17:582–6.
[58] Bard AJ, Faulkner LR. Electrochemical methods: fundamentals and applications. New York: Wiley; 1980.
[59] Devine TM. The mechanism of sensitization of austenitic stainless steel. Corros Sci 1990;30:135–51.
[60] Staicopolus DN. The role of cementite in the acidic corrosion of steel. J Electrochem Soc 1963;110:1121–4.
[61] Streicher MA. General and intergranular corrosion of austenitic stainless steels in acids. J Electrochem Soc 1959;106:161–80.
[62] Armijo JS. Intergranular corrosion of nonsensitized austenitic stainless steels; part 1 — environmental variables. Corrosion (NACE) 1965;21:235–44.
[63] Schweitzer PA. Corrosion of stainless steels. Fundamentals of metallic corrosion, atmospheric and media corrosion of metals (Corrosion Engineering Handbook). Boca Raton: CRC Press; 2007 114–6.
[64] Kasparova OV, Baldokhin YV. New concept of the mechanism of intergranular corrosion of stainless steels. Prot Met 2007;43:235–40.
[65] Tedmon CS, Vermilyea DA, Rosolowski JH. Intergranular corrosion of austenitic stainless steel. J Electrochem Soc 1971;118:192–202.
[66] Devine TM. Influence of carbon content and ferrite morphology on the sensitization of duplex stainless steel. MTA 1980;11:791–800.
[67] Hsu H-W, Tsai W-T. High temperature corrosion behavior of siliconized 310 stainless steel. Mater Chem Phys 2000;64:147–55.
[68] Jones DA. Principles and prevention of corrosion. Prentice Hall; 1996.